

SCIENTIFIC REPORTS



OPEN

Light guiding and switching using eccentric core-shell geometries

Ángela I. Barreda¹, Yael Gutiérrez¹, Juan M. Sanz ^{1,2}, Francisco González¹ & Fernando Moreno¹

Received: 12 June 2017

Accepted: 21 August 2017

Published online: 11 September 2017

High Refractive Index (HRI) dielectric nanoparticles have been proposed as an alternative to metallic ones due to their low absorption and magnetodielectric response in the VIS and NIR ranges. For the latter, important scattering directionality effects can be obtained. Also, systems constituted by dimers of HRI dielectric nanoparticles have shown to produce switching effects by playing with the polarization, frequency or intensity of the incident radiation. Here, we show that scattering directionality effects can be achieved with a single eccentric metallo-HRI dielectric core-shell nanoparticle. As an example, the effect of the metallic core displacements for a single Ag-Si core-shell nanoparticle has been analyzed. We report rotation of the main scattering lobe either clockwise or counterclockwise depending on the polarization of the incident radiation leading to new scattering configurations for switching purposes. Also, the efficiency of the scattering directionality can be enhanced. Finally, chains of these scattering units have shown good radiation guiding effects, and for 1D periodic arrays, redirection of diffracted intensity can be observed as a consequence of blazing effects. The proposed scattering units constitute new blocks for building systems for optical communications, solar energy harvesting devices and light guiding at the nanoscale level.

Nanotechnology has revolutionized science of the last decades by generating important theoretical and practical developments. The interaction of electromagnetic radiation with metallic nanoparticles (NPs) has been a vastly investigated field providing applications in many research areas like optics, health, material analysis, communications, biology, etc.¹. When incident radiation excites a metallic NP, free electrons tend to oscillate at the incident radiation frequency, leading to Localized Surface Plasmons (LSPs). These coherent oscillations of the electronic plasma depend on the optical properties of the NP, its size, shape and the wavelength of the impinging light². For certain frequencies, the energy of the incident light is transferred to free electrons, so that they oscillate with maximum amplitude giving rise to resonances in the scattering spectrum. Although in general, metallic NPs exhibit a good response in the spectral range UV-VIS-NIR, their intrinsic Joule's losses limit their plasmonic performance in most of applications^{3,4}. High Refractive Index (HRI) dielectric NPs have been proposed instead as ideal candidates for solving this issue⁵ because light can propagate inside them without being absorbed. In addition, they can present magnetic properties in spite of being non-magnetic materials in nature⁶. So, both electric and magnetic resonances can be observed as a consequence of the excitation of whispering gallery modes⁷. Their spectral position and intensity depend on the NP size, its refractive index and that of the surrounding medium, m_{med} ^{8,9}.

When electric and magnetic spectral resonances overlap, coherence effects appear, leading to a real control of the directionality of the scattered light. This has permitted to redirect the incident radiation in forward, backward or at given scattering angles with respect to the incident direction^{10–12}. Kerker *et al.*¹³ established that, under certain assumptions of the electric permittivity ϵ and magnetic permeability μ , electric and magnetic dipoles can oscillate either in- or out-of-phase. These two situations give rise to special Scattering Directionality Conditions (SDCs), the so-called “zero backward condition” (or First Kerker's condition) and “minimum forward condition” (or Second Kerker's condition) respectively¹⁴.

Recently, symmetric metallo-dielectric or dielectric-dielectric core-shell nanostructures^{15–21} have been studied for improving the scattering directionality properties established by Kerker *et al.*¹³. In particular, by changing the relative size of the core respect to the particle size, it is possible to tune the spectral position of the electric and magnetic resonances and consequently, to govern the above mentioned SDCs^{22,23}. These nanostructures can have applications in solar energy harvesting devices^{24–26}, metamaterials²⁷ or sensing²², among others. More complex

¹Grupo de Óptica, Departamento de Física Aplicada, Universidad de Cantabria, Facultad de Ciencias, Avda. Los Castros s/n, 39005, Santander, Spain. ²Departamento de I+D, Textil Santanderina, S.A., Avenida Textil Santanderina, s/n, 39500, Cabezón de la Sal, Spain. Correspondence and requests for materials should be addressed to F.M. (email: morenof@unican.es)

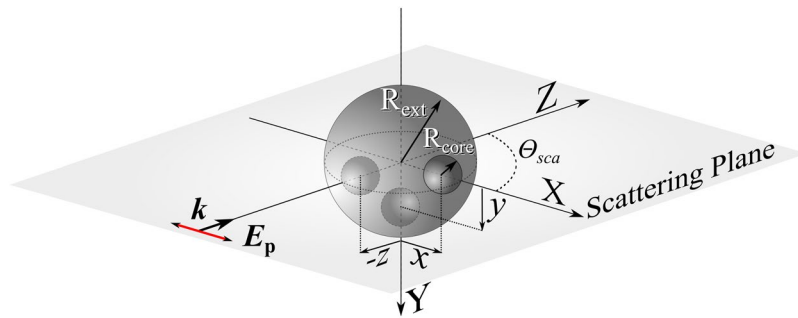


Figure 1. Scattering geometry considered for this study. The core (Ag)-shell (Si) particle has a core radius, R_{core} , and a shell radius, R_{ext} . The structure is illuminated with a monochromatic plane wave with wavevector \mathbf{k} , along the z -axis and polarization, \mathbf{E} , along the x - or y -axis. The three considered displacements are shown by means of the little spheres.

geometries, like dimers, trimers or oligomers have also been explored with the same objective^{28–30}. Moreover, aggregates of particles have also been proposed to redirect the scattered intensity $I(\theta_{\text{sca}})$ into some specific directions respect to that of forward or backward. By means of these structures, it is possible to observe switching effects, whose “on”/“off” states depend on the polarization³¹, frequency^{10,11} or intensity³² of the incident radiation.

Eccentric metallic core-shell nanoparticles (examples are nanorods and nanocups configurations) have been analyzed as new plasmonic units providing with both new spectral tuning possibilities and directionality effects. Near and far-field regimes have been studied. Also, the possibility of manufacturing them in a controlled manner, makes these nanounits very attractive for many application purposes where good tunable plasmonic performance is necessary^{33–36}. Here, we will pay attention to the electromagnetic behavior of eccentric metallo-dielectric core-shell NPs where the shell is made of a HRI dielectric material.

We show that an isolated eccentric core-shell nanoparticle can operate as an optical switching device in a similar way to the one proposed by Barreda *et al.*³¹, based on an homogeneous dimer made of HRI dielectric NPs. However, the eccentric core-shell configuration presents some advantages respect to the dimer, because only one particle is required. The switching effect will also be analyzed at the 90° scattering configuration, which shows clear advantages with respect to the conventional forward and backward directions³⁷.

Another remarkable characteristic of the eccentric core-shell geometry is that, apart from operating as a switching device, it can improve the efficiency of the scattering directionality. In this sense, we demonstrate that there is an optimum core displacement that produces the highest/lowest ratio between the scattered intensities in forward and backward directions for the First/Second Kerker’s condition. By taking advantage of these directionality properties, we have explored the possibility of using aggregates of eccentric core-shell NPs for guiding the incident radiation. A Yagi-Uda type³⁸ light guiding scheme has been studied as an example.

The paper is organized as follows: Firstly, we revisit the SDCs for eccentric Ag-Si core-shell NPs for core displacements along the x - or y -directions, i.e. along the directions perpendicular to that of the propagation, showing a switching effect. Secondly, we analyze the SDCs for core shifts along the propagation direction, improving the efficiency of the scattering directionality patterns. Thirdly, we make a brief discussion of the main results and we evidence the possibility of using aggregates of these eccentric core-shell NPs for guiding applications. Finally, we show the methodology used in this research.

Results

The scattering system is constituted by either isolated or aggregates of eccentric metallo-HRI dielectric core-shell NPs. It is illuminated with a plane wave linearly polarized to either the x - or y -axis and propagating along the z -axis. Its intensity is assumed to be equal to 1. The scattering plane is the z - x and the displacements of the metallic core inside the NP have been considered to be along the three principal axes, as it is shown in Fig. 1. We have focused on Ag-Si core-shell NPs in which the core has been displaced up to 150 nm along the x -, y -, z -axis from its origin. All the electromagnetic study has been carried out by using Multiple Sphere T-matrix Method (MSTM)³⁹ extended to spherical particles with spherical inclusions⁴⁰. We have fixed the external dielectric (Si) shell radius to $R_{\text{ext}} = 230$ nm as in previous studies²². This size has been chosen because dipolar resonances of pure Si NPs are located in a very specific spectral range (1–2 μm)⁶ for radius values between 200–300 nm. This is the spectral range where optical communications devices are commonly designed to operate. Within this region of the spectrum, the imaginary part of the refractive index of pure silicon is negligible, as opposed to what happens in the UV-Visible spectral region⁴¹. On the contrary, the Ag core is highly absorbing and, although the spectral range is far from Ag plasmonic resonances in vacuum^{37,42}, the high permittivity of the shell allows strong plasma oscillations in the wavelength range studied. In spite of the metallic character of the core, the absorption of the incident radiation in the particles takes low values in the analyzed spectral range. In Fig. 2 we show absorption and scattering efficiencies for a concentric Ag-Si core-shell NP as a function of the metallic core size. It is observed how by increasing the metallic core radius respect to particle size, absorption is only slightly increased, being the scattering the dominant contribution, i.e., Ag core is responsible for absorption in that spectral region. In fact, for $R_{\text{core}} = 10$ nm, due to the tiny core size, absorption is negligible as it occurs for pure Si NPs. For eccentric NPs, absorption follows the same behavior, as it can be observed in the Supplementary Note 1, where we show

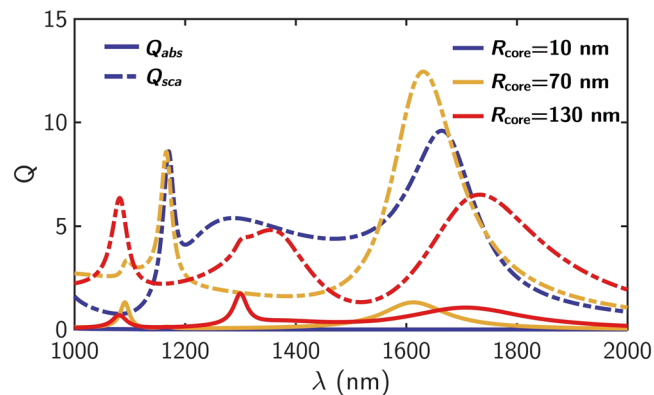


Figure 2. Absorption and scattering efficiencies for a Ag-Si core-shell NP as a function of the core size. Absorption (solid lines) and scattering (dashed lines) efficiencies for various core radii in a Ag-Si core-shell NP ($R_{\text{ext}} = 230$ nm), when it is illuminated by a plane wave propagating along the z -axis and linearly polarized along the x -axis. The values of the analyzed radii are $R_{\text{core}} = 10$ nm, 70 nm and 130 nm (blue, yellow and red lines, respectively).

absorption and scattering efficiencies for both different radii of the metallic core and various shifts along the x -, y - and z -axis.

Revisited Kerker's conditions for eccentric core-shell NPs. In this section we analyze the SDCs for eccentric metallo-dielectric core-shell NPs as a function of the core shift from the NP center along the x -, y - or z -axis. The study has been performed for different core sizes. In particular, we have considered the following cases: $R_{\text{core}} = 10$ nm, 70 nm and 130 nm. Because the electromagnetic response depends on the core displacement direction, we will distinguish two configurations: Shifts of the core either perpendicular or parallel to the propagation direction of the impinging radiation.

Core shifts perpendicular to the propagation direction: Switching effects. In this part we revisit the SDCs for an isolated eccentric Ag-Si core-shell NP whose core has been displaced from the NP center along a direction perpendicular to that of the propagation of the incoming radiation, i.e. along x -axis in Fig. 1. The SDCs have been numerically obtained because, for this particular geometry, it is not possible to get an analytical solution as for the concentric case. For the smallest core size analyzed ($R_{\text{core}} = 10$ nm) both First and Second Kerker's conditions can be fulfilled. In this case, the scattering diagrams are similar to those corresponding to a concentric core-shell NP regardless of the core displacement. This effect comes from the low influence of the metallic core, as it was pointed out in a previous work⁴³. However, for larger core sizes, interesting new effects show up. In fact, when the core displacement is along the x -axis, the scattering diagrams rotate with respect to the concentric case. This effect offers the possibility of redirecting the incident radiation at certain angles with respect to either forward or backward directions (First or Second Kerker's condition, respectively). Also, the rotation is either clockwise or counterclockwise depending on the polarization of the incident radiation and the direction of the shift ($+x$ and $-x$ displacements, see Supplementary Note 2). This behavior can be understood looking at the geometrical anisotropy introduced by the core displacement. Core shifts perpendicular to the incident direction provides similar rotation effects to those obtained with a magneto-optical material (a material whose off-diagonal elements in its dielectric tensor are non-negligible^{44,45}). This means that the effective refractive index of the core-shell NP becomes anisotropic due to the symmetry breaking produced by the core shifting.

As the core size increases, electric resonances are red-shifted while magnetic ones are blue-shifted²². In particular, focusing on the dipolar spectral region, for $R_{\text{core}} = 10$ nm, the magnetic resonance is observed at longer wavelengths than the electric one. Due to the above-mentioned shifts, for $R_{\text{core}} = 70$ nm both resonances appear nearly at the same wavelength. Finally, for $R_{\text{core}} = 130$ nm, the electric dipolar resonance is red-shifted with respect to the magnetic one. Consequently, only the zero-backward condition (First Kerker's condition) can be observed for $R_{\text{core}} = 70$ nm, whilst only the near zero-forward (Second Kerker's condition) is attained for $R_{\text{core}} = 130$ nm^{22,27}.

Figure 3 shows how the maximum scattered intensity at the zero-backward condition ($\lambda = 1685$ nm) is rotated with respect to the forward direction towards either positive or negative angles depending on the polarization of the incident radiation. When the NP is illuminated by a plane wave linearly polarized along the y -axis (s-polarization) the scattering diagram is rotated counterclockwise with respect to the forward direction (see Fig. 3a). On the contrary, when the polarization of the incoming wave is parallel to the core displacement (p-polarization) the rotation is clockwise (see Fig. 3b). The rotation angle depends on the displacement value of the metallic core from the NP center. In Fig. 3c we represent the angle at which the scattered intensity for both s- and p-polarizations is maximum as a function of the core displacement along the x -axis. In particular, the largest rotation is for a displacement of 40 nm, obtaining the maximum scattered intensity at approximately 27° or -28° for s- and p-polarizations respectively. For larger displacements of the core, the SDCs are not longer observed.

As it is shown by means of the shaded gray areas in Fig. 3a,b, it is possible to observe a 120° sector for either s- or p-polarization where the scattered intensity is one order of magnitude lower than in forward direction.

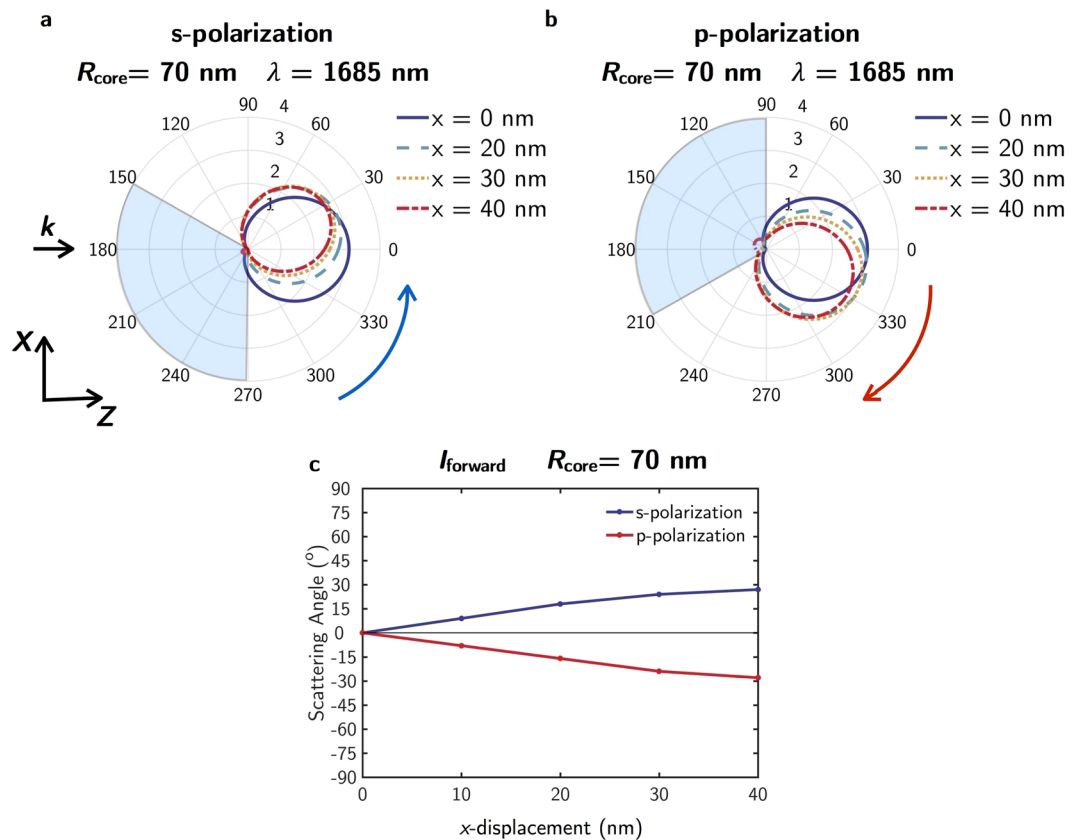


Figure 3. Scattered intensity for $R_{\text{core}} = 70 \text{ nm}$ as a function of the core displacement. Scattering diagrams for the polarizations of the incident radiation (a) perpendicular (s-polarization) and (b) parallel (p-polarization) to the scattering plane (z - x plane in Fig. 1) and different core shifts along the x -axis: 0 nm (blue solid line), 20 nm (blue dashed line), 30 nm (yellow dotted line) and 40 nm (red dash-dotted line). The black arrow labelled with \mathbf{k} indicates the propagation direction of the incident beam. The blue and red arrows refer to the rotation direction. (c) Angle at which the scattered intensity is maximum as a function of the core displacement along the x -axis and s- and p-polarizations of the incident light (blue and red lines respectively).

Figure 4 shows the scattering diagrams for the s- (a) and p-polarization (b) of the incident radiation, and different displacements along the x -axis for $R_{\text{core}} = 130 \text{ nm}$. As stated before, for this core size, only the near zero-forward condition ($\lambda = 1535 \text{ nm}$) is achieved. In fact, for $x = 20 \text{ nm}$, even this condition tends to disappear. Similarly to the case of the zero-backward condition for $R_{\text{core}} = 70 \text{ nm}$, for $R_{\text{core}} = 130 \text{ nm}$, it is possible to observe a rotation of the scattering diagrams at the wavelength where the near zero-forward condition appears, which is clockwise or counterclockwise for s- and p-incident polarization, respectively. Due to this rotation, there is a 50° sector where the scattered intensity is one order of magnitude lower than in backward direction. This region (shaded in grey) is attained for negative or positive angles depending on the polarization of the incident radiation.

This rotation effect makes these structures very promising for switching purposes. By only changing the polarization of the incident radiation, it is possible to go from “on” to “off” states. In particular, we show that the scattered intensity at 90° with respect to the incident direction can be tuned from almost null to maximum values by playing with the polarization of a single frequency excitation and with only an eccentric metallo-dielectric core-shell NP.

In order to show more clearly the above mentioned switching effect, in Fig. 5 we plot $I_s(90^\circ)/I_p(90^\circ)$, the ratio between the scattered intensity at 90° for s- and p-incident polarizations and the wavelengths corresponding to the two SDCs. For both core sizes, 70 nm and 130 nm, as the displacement of the core along the x -axis increases, that ratio takes larger values. In particular, for $R_{\text{core}} = 70 \text{ nm}$ (Fig. 5a) we obtain a ratio of 3.5 for a displacement of $x = 40 \text{ nm}$. For $R_{\text{core}} = 130 \text{ nm}$, the ratio for the largest displacement, $x = 20 \text{ nm}$, is 4.5. These results demonstrate that by swapping the polarization of the exciting radiation from s to p, and fixing a minimum intensity threshold (which will be considered as the “off” state of the device), the scattered radiation at 90° can go from “on” to “off” states. Detecting at 90° is a good way to avoid any parasitic effect due to the incident radiation. In addition, incident polarization is conserved in the scattered radiation when the core shifts are in the scattering plane. Note that results for displacements along the x/y -axis and p/s-polarizations are equivalent to those corresponding to y/x -axis and s/p-polarizations.

Core shifts parallel to the propagation direction: Improving the SDCs. In this section we analyze the electromagnetic behavior of eccentric core-shell NPs when the core displacement is along the z -axis (along the propagation

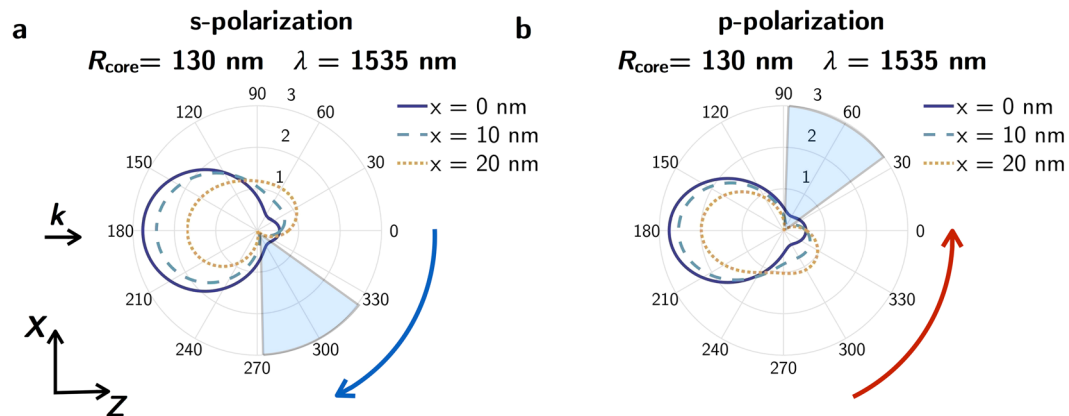


Figure 4. Scattered intensity for $R_{\text{core}} = 130$ nm as a function of the core displacement. Scattering diagrams for the polarizations of the incident radiation (a) perpendicular (s-polarization) and (b) parallel (p-polarization) to the scattering plane (z - x plane in Fig. 1) for different core shifts along the x -axis: 0 nm (blue solid line), 10 nm (blue dashed line) and 20 nm (yellow dotted line). The black arrow labelled with k indicates the propagation direction of the incident beam. The blue and red arrows refers to the rotation direction.

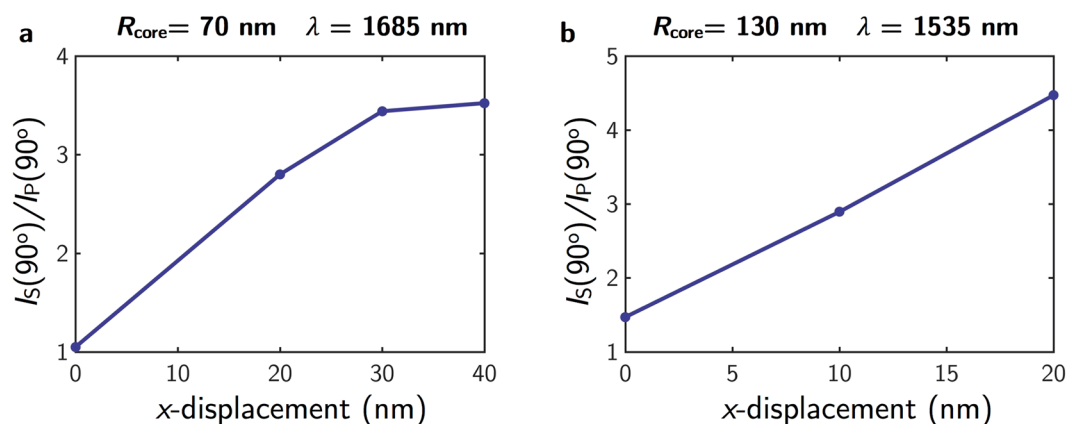


Figure 5. Ratio I_s/I_p at 90° scattering angle. $I_s(90^\circ)/I_p(90^\circ)$ as a function of the core displacement along the x -axis for different core sizes for the wavelengths corresponding to the two SCDs. (a) $R_{\text{core}} = 70$ (First Kerker's condition) nm and (b) $R_{\text{core}} = 130$ nm (Second Kerker's condition) respectively.

direction). In this case, the rotation is not longer achieved because there are no breaks in the symmetry of the problem with respect to either the x - or y -axis, i.e. with respect to p- or s-polarization directions (results are identical for both polarizations of the incident radiation, p and s). However, directionality effects can still be observed. In order to enhance these effects on the analyzed nanostructures, we have looked for the core displacement that produces the highest/lowest ratio between the integrated scattered intensity in the forward and backward angular regions at the First/Second Kerker's condition for all the analyzed core sizes: $R_{\text{core}} = 10$ nm ($\lambda = 1535$ nm, Second Kerker's condition) and ($\lambda = 1820$ nm, First Kerker's condition), $R_{\text{core}} = 70$ nm ($\lambda = 1685$ nm, First Kerker's condition) and $R_{\text{core}} = 130$ nm ($\lambda = 1535$ nm, Second Kerker's condition). See Fig. 6a–c respectively. For $R_{\text{core}} = 10$ nm the ratio is independent of the core displacement. This is because of the small volume of the core in comparison to the volume of the whole particle. Therefore, its influence in the SDCs is negligible⁴³. Results are similar to those corresponding to an isolated particle of radius $R = 230$ nm made of pure silicon. However, for $R_{\text{core}} = 70$ nm, the largest ratio is obtained for $z = +7.5$ nm. For this z -displacement, the integrated scattered intensity in the forward angular region is 14.0 times larger than that scattered in the backward region. This enhances the First Kerker's condition with respect to a concentric core-shell case ($z = 0$ nm). Furthermore, the integrated scattered intensity ratio between forward and backward angular regions is similar to that obtained for the isolated particle (in fact, this value is 14.2). This is shown in Fig. 6a. This suggests that for a particular core size ($R_{\text{core}} = 70$ nm in this case) and a given shift of the metallic core ($z = +7.5$ nm in this case), it is possible to obtain the same results as for a pure Si nanoparticle, where losses are negligible in the analyzed spectral range. This is to say that losses introduced by the metallic core are minimized. For $R_{\text{core}} = 130$ nm, the lowest ratio is observed for $z = +20$ nm. In this case, the intensity scattered in the forward angular region is 0.15 times smaller than that scattered in the backward direction. This enhances the Second Kerker's condition with respect to the concentric core-shell case.

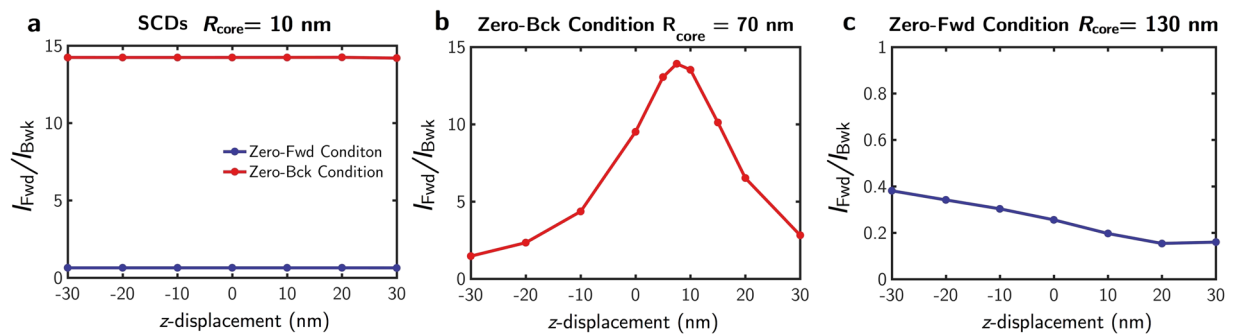


Figure 6. Integrated intensity ratios. Ratio between the integrated scattered intensity in the forward ($\theta_{\text{sca}} \in [-90^\circ, 90^\circ]$) and backward angular regions ($\theta_{\text{sca}} \in [90^\circ, 270^\circ]$) as a function of the core displacement along the z -axis for different core sizes on the First/Second Kerker's condition. (a) $R_{\text{core}} = 10$ nm, (b) $R_{\text{core}} = 70$ nm and (c) $R_{\text{core}} = 130$ nm.

Discussion

The influence of shifting the metallic core in a metal-HRI dielectric (Ag-Si for the analyzed case) core-shell NP has been deeply analyzed. For practical purposes linked to telecommunications applications, the external radius has been fixed to $R_{\text{ext}} = 230$ nm while the core size (R_{core}) has been varied from 10 nm to 130 nm. We have studied the scattering properties of these scattering units by looking at the angular distribution of the scattered intensity in the far-field. For the smallest core size (10 nm) it is not observed any significant change due to the smallness of the core in comparison to the size of the whole particle, 460 nm. However, as the core size increases, some interesting properties arise for the different core displacements. For core displacements perpendicular to the propagation direction of the incoming radiation, a rotation of the SDCs is observed. Its direction depends on the polarization of the incident radiation. In particular, for $R_{\text{core}} = 70$ nm, the rotation of the scattering diagrams at the First Kerker's condition is clockwise for p-incident polarization and counterclockwise for s-incident polarization. The opposite behaviour is found for $R_{\text{core}} = 130$ nm, being the rotation at the Second Kerker's condition counterclockwise for p-incident polarization and clockwise for s-incident polarization. This rotation effect, which is only manifested for the largest core sizes, makes eccentric metallo-dielectric core-shell NPs interesting scattering units for redirecting the incident radiation in the desired angular range and also for building optical switching devices. The switching effect has been quantified by the ratio of the scattered intensity at 90° for the analyzed incident polarizations, either s or p. The large values obtained for $I_s(90^\circ)/I_p(90^\circ)$ demonstrate that by swapping the polarization of the impinging radiation from s to p, and fixing a minimum intensity threshold ("off" state), the scattered radiation at 90° could go from "on" to "off" states.

The fact that only the First or Second Kerker's conditions can be obtained for $R_{\text{core}} = 70$ nm or $R_{\text{core}} = 130$ nm is due to the red-shift and blue-shift undergone by the electric and magnetic resonances as the core size increases, respectively.

Concerning core displacements parallel to the propagation direction, for certain z -axis shifts, the efficiency of the SDCs can be enhanced. In fact, the ratio between the integrated scattered intensity in the forward and backward angular regions can reach the highest/lowest value for $z = 7.5$ nm/ $z = 20$ nm and $R_{\text{core}} = 70$ nm/ $R_{\text{core}} = 130$ nm for the wavelength where the First/Second Kerker's condition is observed.

In order to enhance the analyzed effects, aggregates of the studied eccentric NPs can be used to build nano-antennas for switching and radiation guiding at the nanoscale. To explore this possibility, we have envisaged two types of configurations: chains of up to 6 particles in different spatial distributions and 1D periodic arrays. For the former, this number of particles has been chosen to maintain reasonable directionality and switching conditions as well as to enhance the scattered intensity (see Supplementary Note 3 for further details). Each core-shell NP in the chain has an external and core radius of $R_{\text{ext}} = 230$ nm and $R_{\text{core}} = 70$ nm, respectively. The core has been displaced 30 nm along the x -direction.

In Fig. 7a, the near field map corresponding to a V-shaped chain of 6 particles at the wavelength where the Zero-Backward condition ($\lambda = 1685$ nm) holds for the isolated particle is shown. The inset shows the spatial configuration of the particles. The angle between segments of aligned NPs has been chosen to be $\theta = 20^\circ$ in order to take advantage of the rotation observed in the scattering diagrams of an isolated core-shell NP (see Fig. 3c). The distance between the particles is 137 nm in analogy with a previous work⁴⁶. Figure 7b plots the angular distribution of the far-field scattered intensity for both p- and s-incident polarizations at $\lambda = 1685$ nm (wavelength where the First Kerker's condition holds for the isolated particle). The inset of Fig. 7b plots the far-field observation of the total scattered intensity, within a solid angle of 30° , for p-polarized incident radiation.

In Fig. 7, it can be seen how this chain of particles is able to interact with the impinging radiation maintaining a good intensity enhancement and narrow scattering patterns. Obviously, these structures are more complex than isolated eccentric NPs, but this is balanced with the scattered intensity gain (mainly in p-/s-polarization for z - x / z - y -plane geometries respectively, see Supplementary Note 3) and the strong and narrow scattering patterns. Regarding the values of the scattered intensity, they are higher for the antenna than for the isolated core-shell due to the larger number of NPs that contribute to the scattered radiation. The fact that incident radiation can be guided into the desired direction through aggregates of eccentric core-shell NPs evidences the great potential directionality properties of these nanostructures, opening a door to new antenna designs.

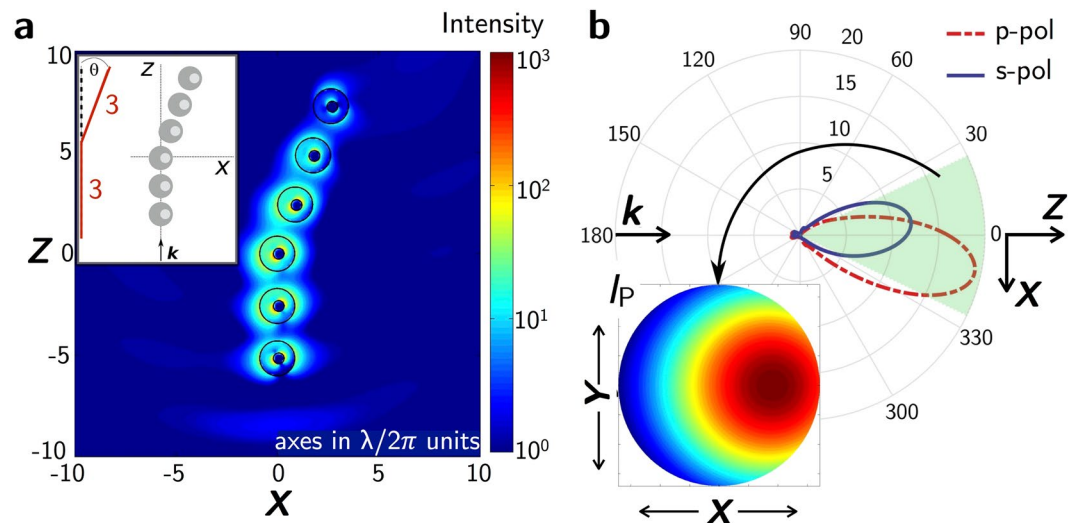


Figure 7. Near- and far-field behaviour of a chain of particles. **(a)** shows near field map of a V-shaped chain of 6 core-shell (Ag-Si) nanoparticles of radii $R_{\text{ext}} = 230$ nm and $R_{\text{core}} = 70$ nm with the core displaced 30 nm along the x -axis. Inset is a scheme of the geometry. The distance between the particles along the x -axis is 137 nm. The angle between segments of aligned NPs is $\theta = 20^\circ$ (see inset in **(a)**). The structure is illuminated with a plane wave propagating along the z -axis and polarized along the x -axis (p-polarization). The plot corresponds to the z - x plane for the wavelength where the Zero-Backward condition holds for the isolated particle. **(b)** Scattering diagrams in the z - x plane for p-incident polarization (red dashed-dotted line) and s-incident polarization (blue solid line) at the First Kerker's condition for the geometry shown in the inset of **(a)**. Inset shows far-field observation of the normalized total scattered intensity, within a solid angle of 30° , for p-polarized incident radiation.

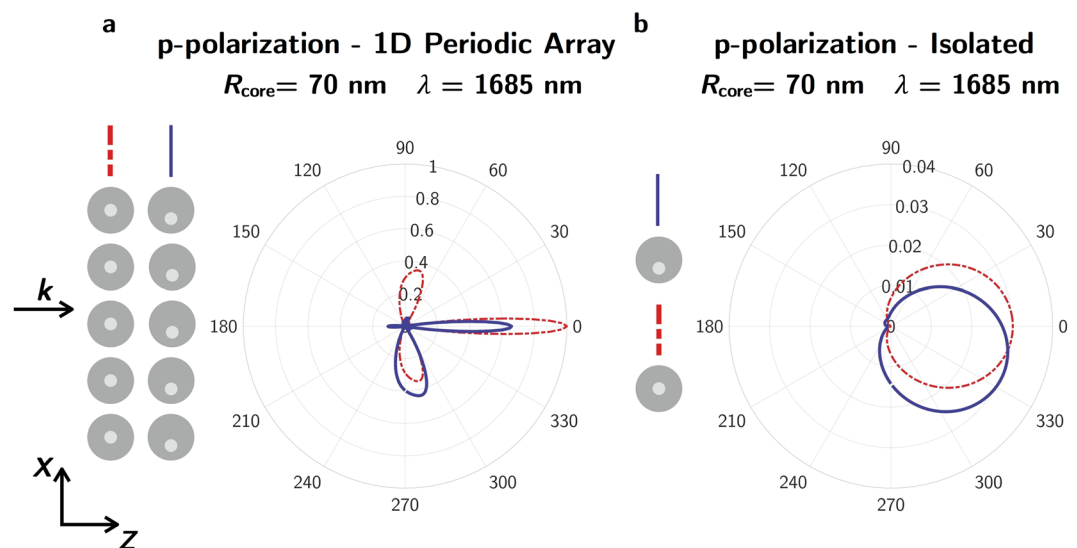


Figure 8. Far-field scattering by a 1D periodic array of eccentric core-shell (Ag-Si) NPs. Scattering diagrams for the polarization parallel to the scattering plane (p-polarization) for: **(a)** five concentric (red dashed-dotted line) and eccentric (solid blue line) core-shell (Ag-Si) NPs in a 1D periodic array configuration with a period of 1711 nm and **(b)** an isolated concentric (red dashed-dotted line) and eccentric (solid blue line) core-shell (Ag-Si) NP. In both cases, $R_{\text{core}} = 70$ nm. For the eccentric case, the core has been shifted 30 nm along the polarization direction (x -axis). The numerical data have been normalized to the maximum intensity scattered by the 1D periodic array structure built with concentric spheres.

Figure 8a shows the far-field scattering patterns of a system built with 5 core-shell NPs (Ag-Si, $R_{\text{ext}} = 230$ nm and $R_{\text{core}} = 70$ nm), either concentric or eccentric, distributed as a 1D array with a period of 1711 nm. The system is illuminated by a plane wave linearly polarized along the direction that connects the NPs, p-incident polarization. For the eccentric core-shells, the core has been shifted 30 nm along the polarization direction. This 1D periodic array configuration tries to mimic a periodic diffraction grating. For comparison, it is also shown the scattering patterns of the corresponding isolated particles, Fig. 8b. Using this 1D periodic array of eccentric

NPs, it is possible to obtain a “blazing” effect and, consequently, a redirectionality of the diffracted radiation due to the scattering anisotropy of the isolated particle. A narrowing of the scattering pattern lobes is expected as the number of array elements is increased.

Finally, it is important to point out that the synthesis of isolated eccentric core-shells^{47,48} and the fabrication of periodic arrays made of either homogeneous⁴⁹ or inhomogeneous^{33,34} (including both concentric and eccentric core-shells) has already been achieved. However, the construction of these antennas remains a challenge since it needs a precise alignment of the cores and particles.

Methods

Lorenz-Mie theory. According to the Lorenz-Mie theory⁵⁰, the incident field can be expanded into vector spherical harmonics. Two cases can be considered, one in which the electric field is polarized perpendicular to the scattering plane ($E_{s,inc}$) and one in which the electric field lies within the scattering plane, ($E_{p,inc}$). The scattered electric-field components are related to the incident ones via the scattering amplitude matrix:

$$\begin{pmatrix} E_{p,sca} \\ E_{s,sca} \end{pmatrix} \propto \begin{pmatrix} S_2 & S_3 \\ S_4 & S_1 \end{pmatrix} \begin{pmatrix} E_{p,inc} \\ E_{s,inc} \end{pmatrix} \quad (1)$$

In case of homogeneous isotropic non-active spheres S_1 , S_2 , S_3 and S_4 are given by

$$\begin{cases} S_1 = \sum_n \frac{2n+1}{n(n+1)} (a_n \pi_n + b_n \tau_n), \\ S_2 = \sum_n \frac{2n+1}{n(n+1)} (a_n \tau_n + b_n \pi_n), \\ S_3 = S_4 = 0 \end{cases} \quad (2)$$

where π_n and τ_n are the angular functions, and a_n , b_n are the so-called Lorenz-Mie scattering coefficients, i.e. the weights of electric and magnetic modes, respectively, that appear in the linear expansion of vector spherical harmonics and indicate the strength of the multipolar contributions of order n . These coefficients depend on the electric and magnetic properties of the particle, on the surrounding medium and on the size parameter $x = 2\pi R m_{med}/\lambda$, where λ is the wavelength of the incident light in vacuum and R is the radius of the spherical particle. In particular, a_1 and b_1 correspond to the electric and magnetic dipolar modes and a_2 and b_2 to the quadrupolar ones, respectively.

The total scattered intensities with polarization parallel, $I_p(\theta_{sca})$, and perpendicular, $I_s(\theta_{sca})$, to the scattering plane are proportional to $|S_2(\theta)|^2$ and $|S_1(\theta)|^2$, respectively, whereas extinction and scattering efficiencies are given by:

$$\begin{aligned} Q_{ext} &= \frac{2}{x^2} \sum_{n=1}^{\infty} (2n+1) \text{Re}\{a_n + b_n\} \\ Q_{sca} &= \frac{2}{x^2} \sum_{n=1}^{\infty} (2n+1) (|a_n|^2 + |b_n|^2) \end{aligned} \quad (3)$$

Nevertheless, eccentric core-shell NPs are a particular case of spherical NPs and cannot be analyzed as homogeneous non-active isotropic spheres^{51–53}, in such a way that S_3 and S_4 can be different from 0, depending on the scattering direction and system geometry. A deeper theoretical analysis to obtain the scattering amplitude matrix elements in such systems is avoided, since MSTM gives conspicuous results. Further details about scattering theory of anisotropic spheres can be found in the bibliography^{54,55}.

MSTM and FEM. The scattering patterns at different wavelengths and for both analyzed polarizations of the incident radiation (s and p) have been studied by using the T-matrix method³⁹. T-matrix is one of the most powerful and widely used tools for accurately computing light scattering by particles, both isolated and aggregated, based on directly solving Maxwell’s equations. In this method, the field external to the cluster of N -spheres (\mathbf{E}_{sca}) is represented by the superposition of the incident (\mathbf{E}_{inc}) and scattered fields, and the scattered field consists of components radiated from each sphere in the target ($\mathbf{E}_{sca,i}$):

$$\mathbf{E}_{sca} = \mathbf{E}_{inc} + \sum_{i=1}^{N_{tot}} \mathbf{E}_{sca,i} \quad (4)$$

Incident and scattered fields can be represented by regular and outgoing vector spherical wavefunction expansions, leading to an extension of Lorenz-Mie theory to the multiple sphere system. Application of the proper continuity equations at the surface of each sphere results in a system of interaction equations for the scattered field coefficients, where the boundaries are in the form of closed spherical surfaces⁵⁶. Although the code allows for Gaussian Beam incidence, all calculations have been done using plane waves, to avoid singularities and misunderstandings related to scattering patterns.

In the case of the 1D periodic arrays, the electromagnetic simulations have been made by means of the Finite Element Method (FEM) implemented on the commercial software COMSOL Multiphysics⁵⁷. In particular, we used the RF Module that allows us to formulate and solve the differential form of Maxwell’s equations together with the initial and boundary conditions. The equations are solved using the finite element method with numerically stable edge element discretization in combination with state-of-the-art algorithms for preconditioning and

solution. A spherical region of embedding medium around the NP is also modeled, whose radius is larger than a wavelength. A perfectly matched layer (PML) domain is outside of the embedding medium domain and acts as an absorber of the scattered field. The mesh was fine enough as to allow convergence of the results.

References

- Prasad, P. *Nanophotonics*. (John Wiley & Sons, Inc., Hoboken, New Jersey, 2004).
- Kelly, K. L., Coronado, E., Zhao, L. L. & Schatz, G. The optical properties of metal nanoparticles: the influence of size, shape and dielectric environment. *J. Phys. Chem. B* **107**, 668 (2003).
- Maier, S. A. *Plasmonics: Fundamentals and Applications* (Springer, New York, 2007).
- Sanz, J. M. *et al.* UV plasmonic behavior of various metal nanoparticles in the near- and far-field regimes: Geometry and substrate effects. *J. Phys. Chem. C* **117**, 19606–19615 (2013).
- Caldarola, M. *et al.* Non-plasmonic nanoantennas for surface enhanced spectroscopies with ultra-low heat conversion. *Nat. Commun.* **6**, 7915 (2015).
- García-Etxarri, A. *et al.* Strong magnetic response of submicron silicon particles in the infrared. *Opt. Express* **19**, 4815–4826 (2011).
- Mazumder, M. M., Chowdhury, D. Q., Hill, S. C. & Chang, R. K. Optical resonances of a spherical dielectric microcavity: Effects of perturbations. *Optical Processes In Microcavities* **3**, 209–256 (1996).
- Barreda, A. I., Sanz, J. M. & González, F. Using linear polarization for sensing and sizing dielectric nanoparticles. *Opt. Exp.* **23**, 9157–9166 (2015).
- Tribelsky, M. I., Geffrin, J. M., Litman, A., Eyraud, C. & Moreno, F. Small dielectric spheres with high refractive index as new multifunctional elements for optical devices. *Sci. Rep.* **5**, 12288 (2015).
- Albella, P., Shibamura, T. & Maier, S. A. Switchable directional scattering of electromagnetic radiation with subwavelength asymmetric silicon dimers. *Sci. Rep.* **5**, 18322 (2015).
- Shibamura, T. *et al.* Experimental demonstration of tunable directional scattering of visible light from all-dielectric asymmetric dimers. *ACS Photonics* **4**, 489–494 (2017).
- Shibamura, T., Albella, P. & Maier, S. A. Unidirectional light scattering with high efficiency at optical frequencies based on low-loss dielectric nanoantennas. *Nanoscale* **8**, 14184–14192 (2016).
- Kerker, M., Wang, D. S. & Giles, C. L. Electromagnetic scattering by magnetic spheres. *J. Opt. Soc. Am.* **73**, 765–767 (1983).
- Geffrin, J. M. *et al.* Magnetic and electric coherence in forward-and back-scattered electromagnetic waves by a single dielectric subwavelength sphere. *Nat. Commun.* **3**, 1171 (2012).
- Ruffino, F. *et al.* Novel approach to the fabrication of Au/silica core-shell nanostructures based on nanosecond laser irradiation of thin Au films on Si. *Nanotechnology* **23**, 045601 (2012).
- Ruffino, F., Pugliara, A., Carria, E., Bongiorno, C. & Grimaldi, M. Light scattering calculations from Au and Au/SiO₂ core/shell nanoparticles. *Ph. E: Low-dimensional Systems and Nanostructures* **47**, 25–33 (2013).
- Tsuchimoto, Y. *et al.* Controlling the visible electromagnetic resonances of Si/SiO₂ dielectric core-shell nanoparticles by thermal oxidation. *Small* **11**, 4844–4849 (2015).
- Naraghi, R., Sukhov, S. & Dogariu, A. Directional control of scattering by all-dielectric core-shell spheres. *Opt. Lett.* **40**, 585–588 (2015).
- Liu, W. Ultra-directional super-scattering of homogenous spherical particles with radial anisotropy. *Opt. Express* **23**, 14734–14743 (2015).
- Liu, W., Oulton, R. F. & Kivshar, Y. S. Geometric interpretations for resonances of plasmonic nanoparticles. *Sci. Rep.* **5**, 12148 (2015).
- Tsuchimoto, Y., Yano, T.-a., Hayashi, T. & Hara, M. Fano resonant all-dielectric core/shell nanoparticles with ultrahigh scattering directionality in the visible region. *Opt. Express* **24**, 14451–14462 (2016).
- Barreda, A. I., Gutiérrez, Y., Sanz, J. M., González, F. & Moreno, F. Polarimetric response of magnetodielectric core-shell nanoparticles: an analysis of scattering directionality and sensing. *Nanotechnology* **27**, 234002 (2016).
- Savelev, R. S., Sergaeva, O. N., Baranov, D. G., Krasnok, A. E. & Alù, A. Dynamically reconfigurable metal-semiconductor yagi-uda nanoantenna. *Phys. Rev. B* **95**, 235409 (2017).
- Pillai, S., Catchpole, K. R., Trupke, T. & Green, M. A. Surface plasmon enhanced silicon solar cells. *J. Appl. Phys.* **101**, 093105 (2007).
- Losurdo, M. *et al.* Enhanced absorption in Au nanoparticles/a-Si:H/c-Si heterojunction solar cells exploiting Au surface plasmon resonance. *Sol. Energ. Mat. Sol. Cells* **93**, 1749–1754 (2009).
- Akimov, Y. A., Koh, W. S. & Ostrikov, K. Enhancement of optical absorption in thin-film solar cells through the excitation of higher-order nanoparticle plasmon modes. *Opt. Express* **17**, 10195–10205 (2009).
- Paniagua-Domínguez, R., López-Tejeda, F., Marqués, R. & Sánchez-Gil, J. A. Metallo-dielectric core-shell nanospheres as building blocks for optical three-dimensional isotropic negative-index metamaterials. *New J. Phys.* **13**, 123017 (2011).
- Bakker, R. *et al.* Magnetic and electric hotspots with silicon nanodimers. *Nano Lett.* **15**, 2137–2142 (2015).
- Yan, J. *et al.* Magnetically induced forward scattering at visible wavelengths in silicon nanosphere oligomers. *Nat. Commun.* **6**, 7402 (2015).
- Krasnok, A., Miroshnichenko, A., Belov, P. & Kivshar, Y. All-dielectric optical nanoantennas. *Opt. Express* **20**, 20599–20604 (2012).
- Barreda, A. I. *et al.* Electromagnetic polarization controlled perfect switching effect with high refractive index dimers. the beam-splitter configuration. *Nat. Commun.* **8**, 13910 (2017).
- Baranov, D. G., Makarov, S. V., Krasnok, A. E. & Belov, P. A. & Alù, A. Tuning of near- and far-field properties of all-dielectric dimer nanoantennas via ultrafast electron-hole plasma photoexcitation. *Laser Photon. Rev.* **10**, 1009–1015 (2016).
- Knight, M. W. & Halas, N. J. Nanoshells to nanoevgs to nanocups: optical properties of reduced symmetry core-shell nanoparticles beyond the quasistatic limit. *New J. Phys.* **10**, 105006 (2008).
- Mirin, N. A. & Halas, N. J. Light-bending nanoparticles. *Nano Lett.* **9**, 1255–1259 (2009).
- Wang, H. *et al.* Symmetry breaking in individual plasmonic nanoparticles. *Proc. Natl. Acad. Sci. USA* **103**, 10856–10860 (2006).
- Peña-Rodríguez, O. *et al.* Near- and Far-Field Optical Response of Eccentric Nanoshells. *Nanoscale Res. Lett.* **12**, 16 (2017).
- Curry, A., Nusz, G., Chilkoti, A. & Wax, A. Substrate effect on refractive index dependence of plasmon resonance for individual silver nanoparticles observed using darkfield microspectroscopy. *Opt. Express* **13**, 2668–2677 (2005).
- Li, J., Salandrino, A. & Engheta, N. Shaping light beams in the nanometer scale: A yagi-uda nanoantenna in the optical domain. *Phys. Rev. B* **76**, 245403 (2007).
- Mackowski, D. & Mishchenko, M. A multiple sphere T-matrix fortran code for use on parallel computer clusters. *J. Quant. Spectrosc. Radiat. Transfer* **112**, 2182–2192 (2011).
- Mishchenko, M., Liu, L. & Mackowski, D. Morphology-dependent resonances of spherical droplets with numerous microscopic inclusions. *Opt. Lett.* **39**, 1701–1704 (2014).
- Fu, Y. H., Kuznetsov, A. I., Miroshnichenko, A. E., Yu, Y. F. & Luk'yanchuk, B. Directional visible light scattering by silicon nanoparticles. *Nat. Commun.* **4**, 1527 (2013).
- Gutiérrez, Y. *et al.* How an oxide shell affects the ultraviolet plasmonic behavior of Ga, Mg, and Al nanostructures. *Opt. Express* **24**, 20621–20631 (2016).
- Sanz, J. M. *et al.* Influence of pollutants in the magneto-dielectric response of silicon nanoparticles. *Opt. Lett.* **39**, 3142–3144 (2014).

44. de la Osa, R. A., Albella, P., Saiz, J. M., González, F. & Moreno, F. Extended discrete dipole approximation and its application to bianisotropic media. *Opt. Express* **18**, 23865–23871 (2010).
45. de Sousa, N., Froufe-Pérez, L. S., Sáenz, J. J. & García-Martín, A. Magneto-Optical Activity in High Index Dielectric Nanoantennas. *Sci. Rep.* **6**, 30803 (2016).
46. Krasnok, A. E., Miroschnichenko, A. E., Belov, P. A. & Kivshar, Y. S. Huygens Optical Elements and Yagi–Uda Nanoantennas Based on Dielectric Nanoparticles. *JETP Lett.* **94**, 593–598 (2011).
47. Zhao, Y. *et al.* A simple approach to the synthesis of eccentric Au@SiO₂ janus nanostructures and their catalytic applications. *Surf. Sci.* **648**, 313–318 (2016).
48. Seh, Z. W., Liu, S., Zhang, S.-Y., Shah, K. W. & Han, M.-Y. Synthesis and multiple reuse of eccentric Au–TiO₂ nanostructures as catalysts. *Chem. Commun.* **47**, 6689–6691 (2011).
49. Bakker, R. M., Yu, Y. F. & Paniagua-Domínguez, R. Lu'yanchuk, B. & Kuznetsov, A. I. Resonant light guiding along a chain of silicon nanoparticles. *Nano Lett.* **17**, 3458–3464 (2017).
50. Bohren, C. F. & Huffman, D. R. *Absorption and Scattering of Light by Small Particles*, 2 edn (Wiley-VCH, 2010).
51. Kiselev, A., Reshetnyak, V. & Sluckin, T. Light scattering by optically anisotropic scatterers: *T*-matrix theory for radial and uniform anisotropies. *Phys. Rev. E* **65**, 056609 (2002).
52. Quirantes, A. & Bernard, S. Light scattering by marine algae: two-layer spherical and nonspherical models. *J. Quant. Spectrosc. Radiat. Transfer* **89**, 311 – 321 {VII} Electromagnetic and Light Scattering by Non-Spherical Particles: Theory, Measurement, and Applications (2004).
53. Kahnert, M. Modelling radiometric properties of inhomogeneous mineral dust particles: Applicability and limitations of effective medium theories. *J. Quant. Spectrosc. Radiat. Transfer* **152**, 16–27 (2015).
54. Qiui, C., Li, L., Yeo, T. & Zouhdi, S. Scattering by rotationally symmetric anisotropic spheres: Potential formulation and parametric studies. *Phys. Rev. E* **75**, 026609 (2007).
55. Li, Z., Wu, Z. & Bai, L. Electromagnetic scattering from uniaxial anisotropic bispheres located in a gaussian beam. *J. Quant. Spectrosc. Radiat. Transfer* **126**, 25–30 (2013).
56. Mackowski, D. A general superposition solution for electromagnetic scattering by multiple spherical domains of optically active media. *J. Quant. Spectrosc. Radiat. Transfer* **133**, 264–270 (2014).
57. COMSOL *Multiphysics 5.0* (Comsol Inc., 2015) (<http://www.comsol.com/>).

Acknowledgements

This research was supported by MICINN (Spanish Ministry of Science and Innovation, project FIS2013-45854-P) and Fundación Iberdrola España, Call for Research on Energy and the Environment Grants. Á.I.B. and Y.G. want to express her gratitude to the University of Cantabria for their PhD grants.

Author Contributions

Á.I.B., J.M.S., F.G. and F.M. conceived the original idea. J.M.S. and Á.I.B. carried out numerical calculations. Á.I.B., Y.G., J.M.S., F.G. and F.M. analyzed the results and figures. Á.I.B. and J.M.S. wrote the paper. F.G. and F.M. supervised the study. All authors reviewed the manuscript.

Additional Information

Supplementary information accompanies this paper at doi:[10.1038/s41598-017-11401-y](https://doi.org/10.1038/s41598-017-11401-y)

Competing Interests: The authors declare that they have no competing interests.

Publisher's note: Springer Nature remains neutral with regard to jurisdictional claims in published maps and institutional affiliations.



Open Access This article is licensed under a Creative Commons Attribution 4.0 International License, which permits use, sharing, adaptation, distribution and reproduction in any medium or format, as long as you give appropriate credit to the original author(s) and the source, provide a link to the Creative Commons license, and indicate if changes were made. The images or other third party material in this article are included in the article's Creative Commons license, unless indicated otherwise in a credit line to the material. If material is not included in the article's Creative Commons license and your intended use is not permitted by statutory regulation or exceeds the permitted use, you will need to obtain permission directly from the copyright holder. To view a copy of this license, visit <http://creativecommons.org/licenses/by/4.0/>.

© The Author(s) 2017